Online-only supplement

Primary aldosteronism: spatial multi-omics mapping of genotype-dependent heterogeneity and tumor expansion of aldosterone-producing adenomas

Siyuan Gong, Na Sun†, Lucie S Meyer†, Martina Tetti, Christina Koupourtidou, Stefan Krebs, Giacomo Masserdotti, Helmut Blum, William E. Rainey, Martin Reincke, Axel Walch,
Tracy Ann Williams*

†Na Sun and Lucie S Meyer are co-second authors and contributed equally to this work.

Affiliations: Medizinische Klinik und Poliklinik IV, Klinikum der Universität München, LMU München, München, Germany (S Gong, LS Meyer, M Tetti, M Reincke, TA Williams); Institute of Stem Cell Research, Helmholtz Center Munich, Neuherberg, Germany (G Masserdotti); Department for Cell Biology and Anatomy, Biomedical Center, Ludwig-Maximilians-Universität (LMU), Planegg-Martinsried, Germany (C Koupourtidou); Graduate School Systemic Neurosciences, Ludwig-Maximilians-Universität (LMU), Planegg-Martinsried, Germany (C Koupourtidou); Physiological Genomics, Biomedical Center (BMC), Ludwig-Maximilians-Universität (LMU), Planegg-Martinsried, Germany (G Masserdotti); Laboratory for Functional Genome Analysis, Gene Center, LMU Munich, 81377 Munich, Germany (S Krebs, H Blum); Department of Molecular and Integrative Physiology, University of Michigan, Ann Arbor, Michigan, USA (WE Rainey); Division of Metabolism, Endocrine, and Diabetes, Department of Internal Medicine, University of Michigan, Ann Arbor, Michigan, USA (WE Rainey); Research Unit Analytical Pathology, German Research Center for Environmental Health, Helmholtz Zentrum München, Germany (N Sun, A Walch).

***Corresponding author**: Tracy Ann Williams PhD, Medizinische Klinik und Poliklinik IV, Klinikum der Universität München, LMU München, Ziemssenstr. 5, D-80336 München, Germany.
Tel: +49 89 4400 52137; Fax: +49 89 4400 54428; Email: Tracy.Williams@med.uni-muenchen.de

Table of contents

Supplementary Methods

Supplementary Tables

Supplementary Figures

Expanded Materials and Methods

Patients. Surgically removed adrenals from 7 patients diagnosed with unilateral primary aldosteronism (PA) and with a histopathological classification of an aldosterone-producing adenoma (APA)[1] were used for this study. Patients were diagnosed with unilateral PA according to the Endocrine Society Clinical Practice Guideline[2] implemented into local standard operational procedures.[3] Briefly, the plasma aldosterone-to-direct renin concentration ratio was used for screening and the diagnosis of PA was confirmed by intravenous saline load testing.[2,4] Subtype differentiation of unilateral from bilateral aldosterone hypersecretion was performed by adrenal venous sampling.[3] The correct diagnosis of unilateral PA with aldosterone hypersecretion lateralized to one adrenal gland was confirmed by postsurgical complete biochemical success.[5]

DNA sequencing. CYP11B2-guided Sanger sequencing of formalin-fixed paraffin-embedded (FFPE) resected adrenals was used for mutation analysis.[6] Accordingly, genomic DNA was extracted from APA, and, for confirmation of the somatic origin of identified mutations, DNA was also extracted from the adjacent cortex or peripheral blood leukocytes before DNA Sanger sequencing of *KCNJ5*.[6] When a *KCNJ5* mutation was not detected by Sanger sequencing, extracted DNA was further analyzed for PA-driver mutations using NGS panels.[7]

Tissue sample preparation and quality control. After resection, fresh tumor and paired adjacent adrenal tissue were snap-frozen in liquid nitrogen and stored at −80 °C. Frozen tissues were embedded in optimal cutting temperature compound (Tissue-Tek). For RNA quality control, RNA integrity number (RIN) analysis was determined (2100 Bioanalyzer, Agilent). Samples with a RIN>7 were used for spatial transcriptomics analyses. Consecutive sections of each sample were cut for spatial gene expression slides, CYP11B2 immunohistochemistry and MALDI slides.

Spatial transcriptomics sample preparation and sequencing. Tissue cryosections (10 µm thick) were mounted onto capture areas (6.5 × 6.5 mm) of a pre-chilled Visium tissue optimization slide (Visium, 10x Genomics, PN-1000193) and the optimal tissue permeabilization time was established as 18 min (10x Genomics, CG000238 Rev D). Cryosections (10 µm thick) mounted on capture areas (6.5 × 6.5 mm) of spatial gene expression slides (Visium, 10x Genomics, PN-1000187) were used for hematoxylin and eosin (H&E) staining and bright field imaging (Zeiss Axio Imager M2 microscope) before tissue permeabilization and cDNA library preparation (10X Genomics, CG000239 Rev D). Libraries were sequenced on the Illumina NextSeq1000 platform. The number of bases sequenced were Read 1, 28 cycles; i5 and i7 indexes, 10 cycles; Read 2, 90 cycles.

MALDI-mass spectrometry imaging. Samples were processed for spatial metabolomics analyses by high-mass-resolution in situ MALDI-MSI (matrix assisted laser desorption/ionization-mass spectrometry imaging) as described previously.[8] Cryosections (12 µm thick) were mounted onto indium-tin-oxide-coated glass slides. The matrix solution consisted of 10 mg/mL 9-aminoacridine hydrochloride monohydrate (9-AA) (Sigma-Aldrich, Germany) in water/methanol 30:70 (v/v). A SunCollect automatic sprayer (Sunchrom, Friedrichsdorf, Germany) was used for matrix application. MALDI-MSI measurements were conducted on a Bruker Solarix 7T FT-ICR-MS (Bruker Daltonik, Bremen, Germany) in negative ion mode using 100 laser shots at a frequency of 1,000 Hz. The MALDI-MSI data were acquired over a mass range of *m/z* 75–1,000 with 50 µm lateral resolution. Following MALDI imaging, tissue sections were H&E stained and scanned (AxioScan.Z1 digital slide scanner with a 20x objective, Zeiss, Jena, Germany). The mass spectra underwent root mean square normalization and processed using SCiLS Lab v. 2022 (Bruker Daltonics, Germany).

Immunohistochemistry. Frozen tissues (10 µm thick) were fixed with 70% ethanol for 2 min, washed 3 times with Tris-buffered saline, 0.1% Tween-20 detergent (TBST), before blocking with human antiserum for 1h at room temperature. Sections were incubated with a mouse CYP11B2 monoclonal antibody (1:200, clone 41-17B,[9] a kind gift from Celso E. Gomez-Sanchez, University of Mississippi Medical Center, Jackson, MS) at 4°C overnight, followed by 3 washes with TBST. Endogenous peroxidase activity was blocked with peroxidase suppressor (Thermo Scientific) and immunopositive regions were detected using the Dako REAL EnVision Detection System Peroxidase/DAB Rabbit/Mouse kit (Agilent).

Pre-processing of spatial transcriptomics data. Demultiplexed FASTQs were obtained using je-suite.[10] Gene expression matrices were generated with the Space Ranger pipeline (10x Genomics) with the "-reorient-images" option enabled and human genome reference 2020-A (GRCh38 and Ensembl 98) alignment. STUtility built on top of the Seurat R package was used for subsequent analyses.[11,12] A Seurat object was constructed using the InputFromTable function filtered with the criteria of a total count <100 detected across all spots, gene expressed <5 spots, and spots with a total UMI count <200. Count matrices were further matched for gene types (protein coding genes, TR_V_gene, TR_D_gene, TR_J_gene, TR_C_gene, IG_LV_gene, IG_V_gene, IG_J_gene, IG_C_gene, IG_D_gene).

Deconvolution of spatial transcriptomics data. Each tumor section was scaled and normalized using SCTransform (STUtility) with the top 2,000 most variable genes included. Non-negative matrix factorization (NMF) was performed, and the spatial transcriptomics dataset was deconvoluted for identified factors using RunNMF implemented in STUtility. The number of factors per section was determined by stability and error using consensus NMF with 2000 over-dispersed genes used for the factorization steps (cNMF v1.4 python package; patients 1-7, k = 5, 4, 6, 5, 3, 3, 7) (**Figure S9**). Top contributing genes were selected based on the feature loading matrix and enriched for biological processes using gprofiler2R (organism = "hsapiens", sources = "GO:BP"). The significance of enrichment was defined with the hypergeometric test followed by correction for multiple testing.

Identification of distinct spatial transcriptomics regions across APA. To capture shared spatial transcriptomic regions across all 7 APA, a total of 33 factors identified on all APA were computed by hierarchical clustering, using one minus the Pearson correlation coefficient over all gene scores as a distance metric. Two clusters of signatures were identified in manually identified CYP11B2 expressing regions (*CYP11B2*-type 1 and *CYP11B2*-type 2). The top 100 genes with the highest loading for each signature were calculated as described previously.[13] Briefly, the top 50 genes of each factor were combined and average loadings for each gene were computed. Total loadings for repetitive genes were summarized, original loadings for exclusive genes were retained, and loadings of each gene were divided by the number of metagenes within the signature.

Estimate of functional information of signatures. For the two main signatures (*CYP11B2*-type 1 and *CYP11B2*-type 2), an enrichment analysis was performed on the signature´s top 100 most contributing genes using the enricher function against the 50 hallmark gene sets ($P<0.05$).[14]

Dimensionality reduction of APA and adjacent adrenal cortex. To integrate APA and adjacent adrenal tissue, filtered feature-barcode matrices for each sample were merged and converted into a Seurat object using SCTransform (STUtility) with the same filter criteria as above. Integrated Seurat objects were normalized with SCTransform (parameters: variable.features n = 2,000). To reduce dimensionality, principal component analysis was used with RunPCA and 30 dimensions. PCA correction was performed with harmony package[15] using as covariates the section source. A shared nearest neighbor (SNN) graph was created with FindNeighbors (dims = 1:30), followed by FindClusters to cluster spatial spots with a

Louvain algorithm. Clustering was visualized in a 2D embedding, t-distributed stochastic neighbor embedding (TSNE) was created with RunTSNE using the first 30 principal components. A resolution (0.2) was selected in all groups using the Clustree package.[16]

Deconvolution of APA and adjacent adrenal cortex. To explore spatial organization of APA and adjacent adrenal, NMF was applied to the integrated Seurat object (RunNMF function with nfactors = 3) on the SCTransform normalized data omitting ribosomal protein coding genes. Top contributing genes were selected based on the feature loading matrix and enriched for biological processes using gprofiler2R.

Manual region selection of heterogeneous *CYP11B2* expression spots within *KCNJ5* mutated APA. In a tumor structure with a *KCNJ5* mutation, annotation of spatial transcriptomic (ST) spots was performed using Loupe Browser 6. Briefly, the standardised $\log_{10}$-transformed *CYP11B2* expression in tumour regions was calculated on each tumour slide. High *CYP11B2* expressing tumor ST spots were assigned with an expression level above the median and the low *CYP11B2* expressing tumor ST spots were assigned with an expression level below the median. Non-tumor ST spots were annotated as Non-tumor ST spots. *CYP11B2* annotations were exported into Seurat to calculate differentially expressed genes (with the FindAllMarkers function) and pathway enrichment activities.

Differential expression analyses. Differential expression analyses for high *CYP11B2* expressing and low *CYP11B2* expressing clusters were performed using the FindAllMarkers function with Wilcoxon tests. Differentially expressed genes (DGEs) were filtered with an absolute value average log2FC > 0.25 and a false discovery rate (FDR)-adjusted $P < 0.05$.

Estimate of functional information of high and low *CYP11B2* expressing tumour ST spots. For each ST spot, we estimated signalling pathway activities with PROGENy using the top 1,000 genes of each transcriptional footprint. Input expression matrices were normalised using the SCTransform function.

Bioinformatics and statistical analyses of MALDI–MSI data. Tumor regions were annotated as regions of interest (ROIs) based on CYP11B2 immunostaining. Receiver operating characteristic (ROC) analysis as implemented in SCiLS Lab v. 2022 was performed to find masses which discriminated APA from adjacent adrenal tissue and APA-*KCNJ5*^{WT} from APA-*KCNJ5*^{MUT}. Discriminative masses with an AUC>0.75 were annotated by accurate mass matching in Human Metabolome Database (http://www.hmdb.ca/; ion mode: negative; adduct type: [M−H], [M−H2O−H], [M+Na−2H], [M+Cl], and [M+K−2H]; mass accuracy, ≤4 ppm) and Lipid Maps (https://www.lipidmaps.org/; negative mode: [M−H]- and [M+Cl]-; Mass Tolerance: +/- 0.005 m/z). Pathway analysis was performed with MetaboAnalyst 5.0 (http://www.metaboanalyst.ca) and Kyoto Encyclopedia of Genes and Genomes database (http://www.genome.jp/kegg/).

References

1. Williams TA, Gomez-Sanchez CE, Rainey WE, Giordano TJ, Lam AK, Marker A, Mete O, Yamazaki Y, Zerbini MCN, Beuschlein F, et al. International Histopathology Consensus for Unilateral Primary Aldosteronism. *J Clin Endocrinol Metab*. 2021;106:42-54. doi: 10.1210/clinem/dgaa484
2. Funder JW, Carey RM, Mantero F, Murad MH, Reincke M, Shibata H, Stowasser M, Young WF, Jr. The Management of Primary Aldosteronism: Case Detection, Diagnosis, and Treatment: An Endocrine Society Clinical Practice Guideline. *J Clin Endocrinol Metab*. 2016;101:1889-1916. doi: 10.1210/jc.2015-4061

3. Williams TA, Reincke M. MANAGEMENT OF ENDOCRINE DISEASE: Diagnosis and management of primary aldosteronism: the Endocrine Society guideline 2016 revisited. *Eur J Endocrinol*. 2018;179:R19-R29. doi: 10.1530/EJE-17-0990
4. Mulatero P, Monticone S, Deinum J, Amar L, Prejbisz A, Zennaro MC, Beuschlein F, Rossi GP, Nishikawa T, Morganti A, et al. Genetics, prevalence, screening and confirmation of primary aldosteronism: a position statement and consensus of the Working Group on Endocrine Hypertension of The European Society of Hypertension. *J Hypertens*. 2020;38:1919-1928. doi: 10.1097/HJH.0000000000002510
5. Williams TA, Lenders JWM, Mulatero P, Burrello J, Rottenkolber M, Adolf C, Satoh F, Amar L, Quinkler M, Deinum J, et al. Outcomes after adrenalectomy for unilateral primary aldosteronism: an international consensus on outcome measures and analysis of remission rates in an international cohort. *Lancet Diabetes Endocrinol*. 2017;5:689-699. doi: 10.1016/S2213-8587(17)30135-3
6. Nanba K, Omata K, Else T, Beck PCC, Nanba AT, Turcu AF, Miller BS, Giordano TJ, Tomlins SA, Rainey WE. Targeted Molecular Characterization of Aldosterone-Producing Adenomas in White Americans. *J Clin Endocrinol Metab*. 2018;103:3869-3876. doi: 10.1210/jc.2018-01004
7. Nanba K, Rainey WE, Udager AM. Approaches to Gene Mutation Analysis Using Formalin-Fixed Paraffin-Embedded Adrenal Tumor Tissue From Patients With Primary Aldosteronism. *Front Endocrinol (Lausanne)*. 2021;12:683588. doi: 10.3389/fendo.2021.683588
8. Sun N, Meyer LS, Feuchtinger A, Kunzke T, Knosel T, Reincke M, Walch A, Williams TA. Mass Spectrometry Imaging Establishes 2 Distinct Metabolic Phenotypes of Aldosterone-Producing Cell Clusters in Primary Aldosteronism. *Hypertension*. 2020;75:634-644. doi: 10.1161/HYPERTENSIONAHA.119.14041
9. Gomez-Sanchez CE, Qi X, Velarde-Miranda C, Plonczynski MW, Parker CR, Rainey W, Satoh F, Maekawa T, Nakamura Y, Sasano H, et al. Development of monoclonal antibodies against human CYP11B1 and CYP11B2. *Mol Cell Endocrinol*. 2014;383:111-117. doi: 10.1016/j.mce.2013.11.022
10. Girardot C, Scholtalbers J, Sauer S, Su SY, Furlong EE. Je, a versatile suite to handle multiplexed NGS libraries with unique molecular identifiers. *BMC Bioinformatics*. 2016;17:419. doi: 10.1186/s12859-016-1284-2
11. Parigi SM, Larsson L, Das S, Ramirez Flores RO, Frede A, Tripathi KP, Diaz OE, Selin K, Morales RA, Luo X, et al. The spatial transcriptomic landscape of the healing mouse intestine following damage. *Nat Commun*. 2022;13:828. doi: 10.1038/s41467-022-28497-0
12. Andersson A, Larsson L, Stenbeck L, Salmen F, Ehinger A, Wu SZ, Al-Eryani G, Roden D, Swarbrick A, Borg A, et al. Spatial deconvolution of HER2-positive breast cancer delineates tumor-associated cell type interactions. *Nat Commun*. 2021;12:6012. doi: 10.1038/s41467-021-26271-2
13. Chen YP, Yin JH, Li WF, Li HJ, Chen DP, Zhang CJ, Lv JW, Wang YQ, Li XM, Li JY, et al. Single-cell transcriptomics reveals regulators underlying immune cell diversity and immune subtypes associated with prognosis in nasopharyngeal carcinoma. *Cell Res*. 2020;30:1024-1042. doi: 10.1038/s41422-020-0374-x
14. Hanzelmann S, Castelo R, Guinney J. GSVA: gene set variation analysis for microarray and RNA-seq data. *BMC Bioinformatics*. 2013;14:7. doi: 10.1186/1471-2105-14-7
15. Korsunsky I, Millard N, Fan J, Slowikowski K, Zhang F, Wei K, Baglaenko Y, Brenner M, Loh PR, Raychaudhuri S. Fast, sensitive and accurate integration of single-cell data with Harmony. *Nat Methods*. 2019;16:1289-1296. doi: 10.1038/s41592-019-0619-0
16. Zappia L, Oshlack A. Clustering trees: a visualization for evaluating clusterings at multiple resolutions. *Gigascience*. 2018;7. doi: 10.1093/gigascience/giy083

Table S1. Clinical parameters of surgically treated patients for an aldosterone-producing adenoma.

Parameter	Patient						
	1	2	3	4	5	6	7
Age at surgery (yrs)	35	42	45	56	33	40	43
Sex	Female	Male	Female	Male	Female	Female	Male
BMI (kg/m^2)	21.5	26.4	20.8	25.3	22.9	26.1	26.6
Systolic BP (mmHg)	144	129	173	161	174	142	166
Diastolic BP (mmHg)	96	81	111	81	128	90	103
Anti-HTN meds (DDD)	0.00	0.50	4.00	2.00	0.33	4.00	2.50
Lowest K$^+$ (mmol/L)	3.4	3.7	3.3	3.3	2.7	2.9	3.3
PAC (pg/mL)	108	129	351	198	357	300	262
DRC (mU/L)	2.0	3.0	2.0	2.0	3.1	12.0	3.5
ARR	54	43	176	99	115	25	75
Largest nodule (mm)	14	7	15	7	19	13	17
*G*enotype	KCNJ5-L168R	NMD	KCNJ5-L168R	CACNA1D-L403R	KCNJ5-L168R	NMD	KCNJ5-G151R

Baseline variables of the 7 patients operated for an APA are shown. The defined daily dose (DDD) is the assumed average maintenance dose per day for a drug used for its main indication in adults (https://www.who.int/tools/atc-ddd-toolkit/about-ddd). APA, aldosterone-producing adenoma; ARR, aldosterone-to-renin ratio; BMI, body mass index; BP, blood pressure; DDD, defined daily dose; PAC, plasma aldosterone concentration; DRC, direct renin concentration; HTN, hypertension; K$^+$, potassium ions; KCNJ5, gene encoding potassium inwardly rectifying channel subfamily J member 5; meds, medications; PRA, plasma renin activity; NMD, no mutations detected in *KCNJ5, ATP1A1, ATP2B3, CACNA1D*.

Table S2. **Top 100 genes detected in *CYP11B2*-type 1 and *CYP11B2*-type 2.** Genes are sorted from the highest to the lowest significance.

CYP11B2-type 1		**CYP11B2-type 2**	
Genes 1-50	**Genes 51-100**	**Genes 1-50**	**Genes 51-100**
CYP11B2	LMOD1	FDX1	PAPSS2
HSD3B2	VAT1L	STAR	SLC37A2
PCP4	ATP1B1	CYP11B2	SOAT1
MT3	A2M	HSPE1	HSD3B2
VPREB3	STAR	MT2A	SLC23A2
CYP21A2	VDR	MT3	MT1E
TIMP3	CHCHD10	CYP21A2	RHBDD2
QPCT	PEG10	CYP17A1	FTH1
CCN3	ATP6V1G1	CYP11B1	FTL
KCNJ5	CD81	DHCR24	TUBB
LY6E	DLK1	PPP2R1A	NPTX2
GAPDH	KCNQ1	CYP11A1	LDHB
SMS	ATP1A1	SCARB1	PRKAR2B
FTL	MERTK	SULT2A1	PDK4
FDX1	GPRC5C	GAPDH	MC2R
NPTX2	LSR	CTSA	CTNNB1
COL15A1	ELP1	PCP4	HLA.B
NR4A1	SLC37A2	HIF1A	SQSTM1
PDK4	MC2R	MGST1	B2M
MGP	CPB1	ADGRV1	CBR1
UGCG	EEF1A2	ELP1	TPP1
KCNK3	TSPAN12	CXCR4	PPIF
TSPAN7	SLC6A6	MTCH1	COX17
HOPX	TOMM34	CD55	CCN3
CXCR4	SEC61G	HSPD1	ATP6V1E1
COX20	SELENOW	QPCT	ENO1
VSNL1	MT.ND4L	SH3BP5	RPL26
IGFBP2	MGST1	CD9	RPS27L
WNT4	DNAJC12	ATP6V1G1	BZW1
TPM2	IFITM10	TIMP3	CEBPB
HSPE1	MT.ND2	RPL17	SPARC
LDHB	COX17	TUBB4A	CLU
LSP1	CLRN1	TNFRSF14	CYCS
IGFBP7	CTSA	HSP90B1	KCNK3
ATP2A3	TUBB4A	LY6E	MOB4
MOB4	TBC1D4	COX7B	TOB1
CADM1	CLU	DNAJC12	AKR1B1
RPS27L	TIMP1	PEG10	MDH1
COMMD6	ERN1	TCEAL9	MT.CO3
RAN	TLN1	SLC6A6	TUBB4B
TPP1	PSME2	APOE	SDCBP
SELENOM	NR5A1	CST3	FAM210B
FDXR	RPL26	PKM	CDK2AP2
CTNNB1	CTSB	MCFD2	SLC47A1
ASAH1	PDE2A	ABCB1	MT.CO1
HSPB7	SOD2	FDXR	RDX
SQSTM1	VCAM1	ATP6V0B	PGAM1
CBR1	BEX1	TM7SF2	RPS12
MDH1	RPS12	LDHA	SSR3
MT.ND5	AEBP1	SEC61G	TPM2

Table S3. Discriminative pathways distinguish APA-*KCNJ5*^{WT} and APA-*KCNJ5*^{MUT}

Pathways	-LOG10(p)	Impact
Linoleic acid metabolism	3.916	0
Biosynthesis of unsaturated fatty acids	3.8513	0
Glycerophospholipid metabolism	2.8884	0.39907
Glyoxylate and dicarboxylate metabolism	2.2126	0.03175
D-Glutamine and D-glutamate metabolism	2.1061	1
alpha-Linolenic acid metabolism	1.4358	0.33333
Butanoate metabolism	1.3197	0
Glycerolipid metabolism	1.2682	0.01246
Tryptophan metabolism	1.1446	0.07848
Ether lipid metabolism	1.0943	0
Citrate cycle (TCA cycle)	1.0943	0.13536
Primary bile acid biosynthesis	1.0261	0.00977
Pentose phosphate pathway	1.0223	0.11955
Glycolysis / Gluconeogenesis	0.89954	0.14277
Alanine, aspartate and glutamate metabolism	0.84663	0.19712
Glycine, serine and threonine metabolism	0.73301	0.0058
Arginine and proline metabolism	0.63993	0.086

Table shows pathway enrichment analysis for metabolites identified by MALDI-MSI.

Table S4. Discriminative pathways distinguish APA-*KCNJ5*^{MUT} and adjacent adrenal cortex

Pathways	-LOG10(p)	Impact
Pentose phosphate pathway	6.1792	0.5836
Pentose and glucuronate interconversions	3.6621	0.42186
D-Glutamine and D-glutamate metabolism	1.4327	1
Ascorbate and aldarate metabolism	1.1919	0.5
Arginine biosynthesis	0.76917	0.11675
Alanine, aspartate and glutamate metabolism	0.73024	0.42068
Histidine metabolism	0.6782	0
Pantothenate and CoA biosynthesis	0.5676	0.02143
Glutathione metabolism	0.34877	0.27562
Purine metabolism	0.33342	0.02277
Amino sugar and nucleotide sugar metabolism	0.22226	0.04254
Arginine and proline metabolism	0.21166	0.086
Aminoacyl-tRNA biosynthesis	0.13074	0

Table shows pathway enrichment analysis for metabolites identified by MALDI-MSI

Table S5. Discriminative pathways distinguish APA-*KCNJ5*^{WT} and adjacent adrenal cortex, related to Figure 4F

Pathways	-LOG10(p)	Impact
Linoleic acid metabolism	3.064	0
Amino sugar and nucleotide sugar metabolism	2.9687	0.44731
Fructose and mannose metabolism	2.7998	0.59558
Biosynthesis of unsaturated fatty acids	1.6622	0
Glycolysis / Gluconeogenesis	1.5506	0.08444
Phosphatidylinositol signaling system	1.4439	0.05631
Inositol phosphate metabolism	1.347	0.12365
Starch and sucrose metabolism	1.3388	0.29163
Valine, leucine and isoleucine biosynthesis	1.3148	0
Pentose phosphate pathway	1.1193	0.13892
alpha-Linolenic acid metabolism	0.93353	0.33333
Galactose metabolism	0.91036	0.04375
Pentose and glucuronate interconversions	0.70338	0.14062
Glycerophospholipid metabolism	0.6461	0.33882
Valine, leucine and isoleucine degradation	0.5589	0.04154
N-Glycan biosynthesis	0.24475	0.00676
Primary bile acid biosynthesis	0.19857	0.00977
Aminoacyl-tRNA biosynthesis	0.18278	0

Table shows pathway enrichment analysis for metabolites identified by MALDI-MSI.

Table S6. Differentially expressed steroidogenesis enzyme genes between subpopulations.

	APA-like-1 versus APA-like-2 in patients with *KCNJ5* mutation			**APA-like-3 versus other subpopulations in patients without *KCNJ5* mutation**		
	avg_log$_2$FC	**p-value**	**Adjusted p-value**	**avg_log2FC**	**p-value**	**Adjusted p-value**
CYP11B2	1.711878629	0	0	3.498849164	1.8047E-252	2.44E-248
CYP17A1	0.583643006	1.66E-106	2.24E-102	-1.354281505	1.5088E-211	2.0389E-207
CYP11B1	0.311975826	5.23E-32	7.07E-28	-1.328623301	1.6772E-204	2.2664E-200

avg_log$_2$FC, log fold-change of the average expression between the groups. Positive values indicate higher expression in the former group. The data refer to subpopulations annotated in Figure 6 (main manuscript).

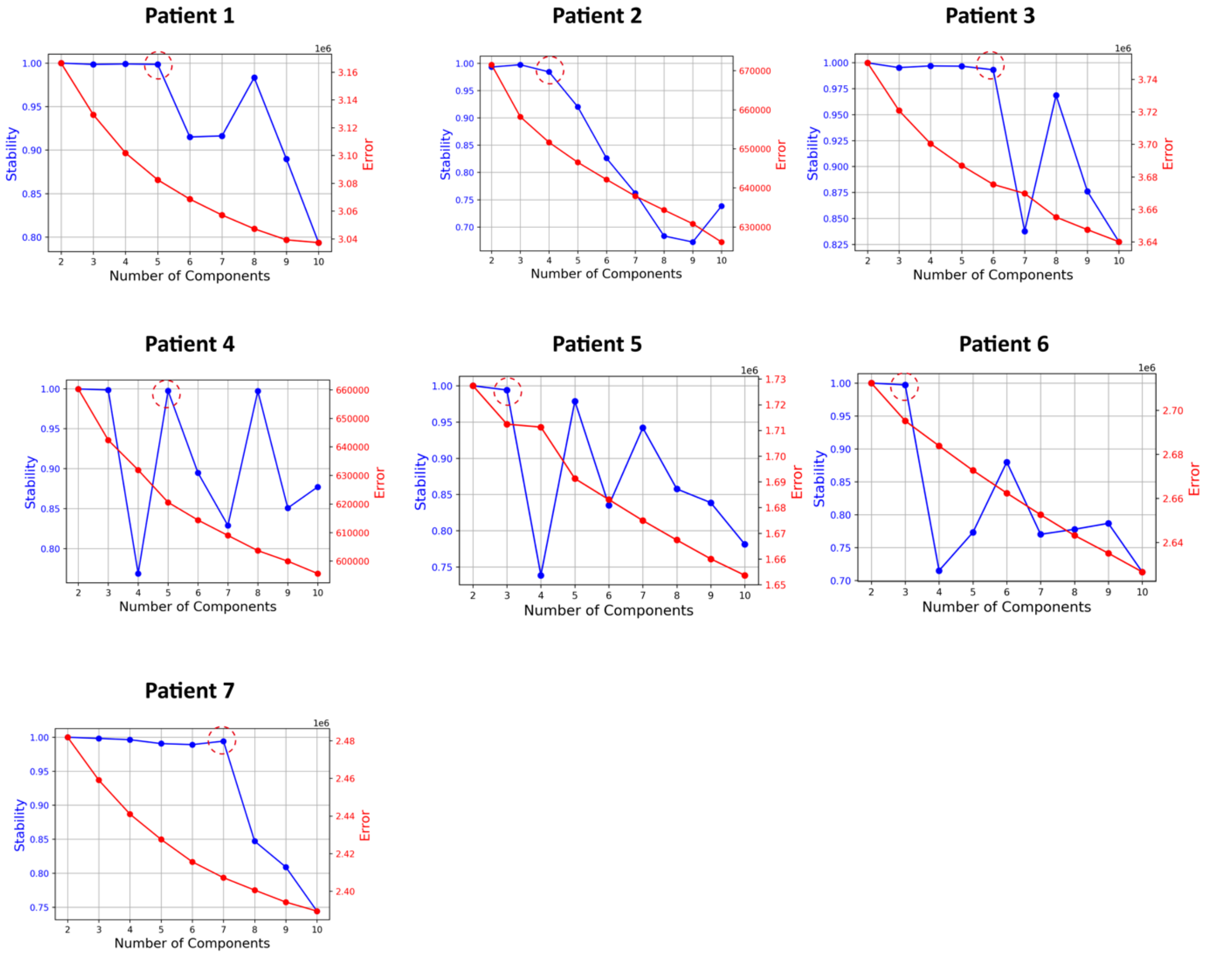
Patient 1

Patient 2

Patient 3

Patient 4

Patient 5

Patient 6

Patient 7

Figure S1. Identification of transcriptionally distinct regions by stability and error using consensus non-negative matrix factorization.

Consensus non-negative matrix factorisation (cNNMF) was used to quantify the optimal number of factors preferentially co-expressed by subsets of spatial transcriptomics spots representing transcriptionally distinct regions within each of the 7 adrenal sections with an APA. Factor number determination for each patient is based on the largest value that is reasonably stable and/or a local maximum in stability and a balance between stability and error, as shown by the dashed circles. By the stability of the solution (as captured by the silhouette score; in blue, left axis) and the Frobenius reconstruction error (in red, right axis) using consensus non-negative matrix factorisation, patients 1 to 7 displayed 5, 4, 6, 5, 3, 3, 7 transcriptionally distinct regions in the adrenal sections.

Patient 1 - *KCNJ5* mutated APA

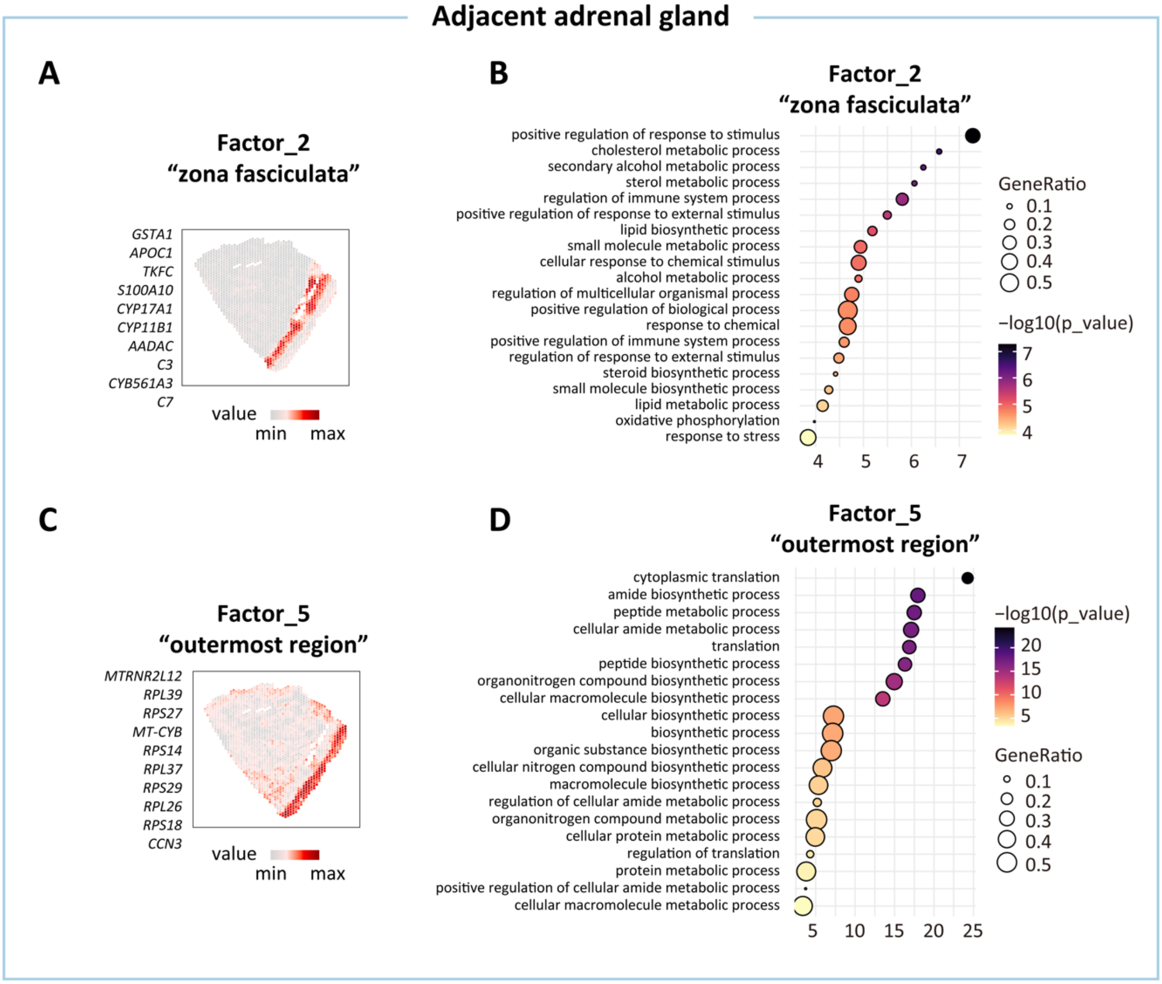

Figure S2. Non-negative matrix factorization reveals distinct molecular patterns in the adjacent adrenal gland of APA with a *KCNJ5* mutation

A and **C**, Spatial distribution of the nontumor-related factors and top 10 genes annotated in the diverse factors. Color-codes indicate gene expression levels. Factor 2 was characterized by zonation markers of zona fasciculata (e.g., *CYP17A1* and *CYP11B1*), whereas factor 5 histologically defined structures that resembled outermost region of the adrenal gland adjacent to an APA. **B** and **D**, Geno Ontology analysis showing enriched biological processes associated with factors related to "zona fasciculata" (factor 2, **Panel A**) and "outermost region" (factor 5, **Panel C**).

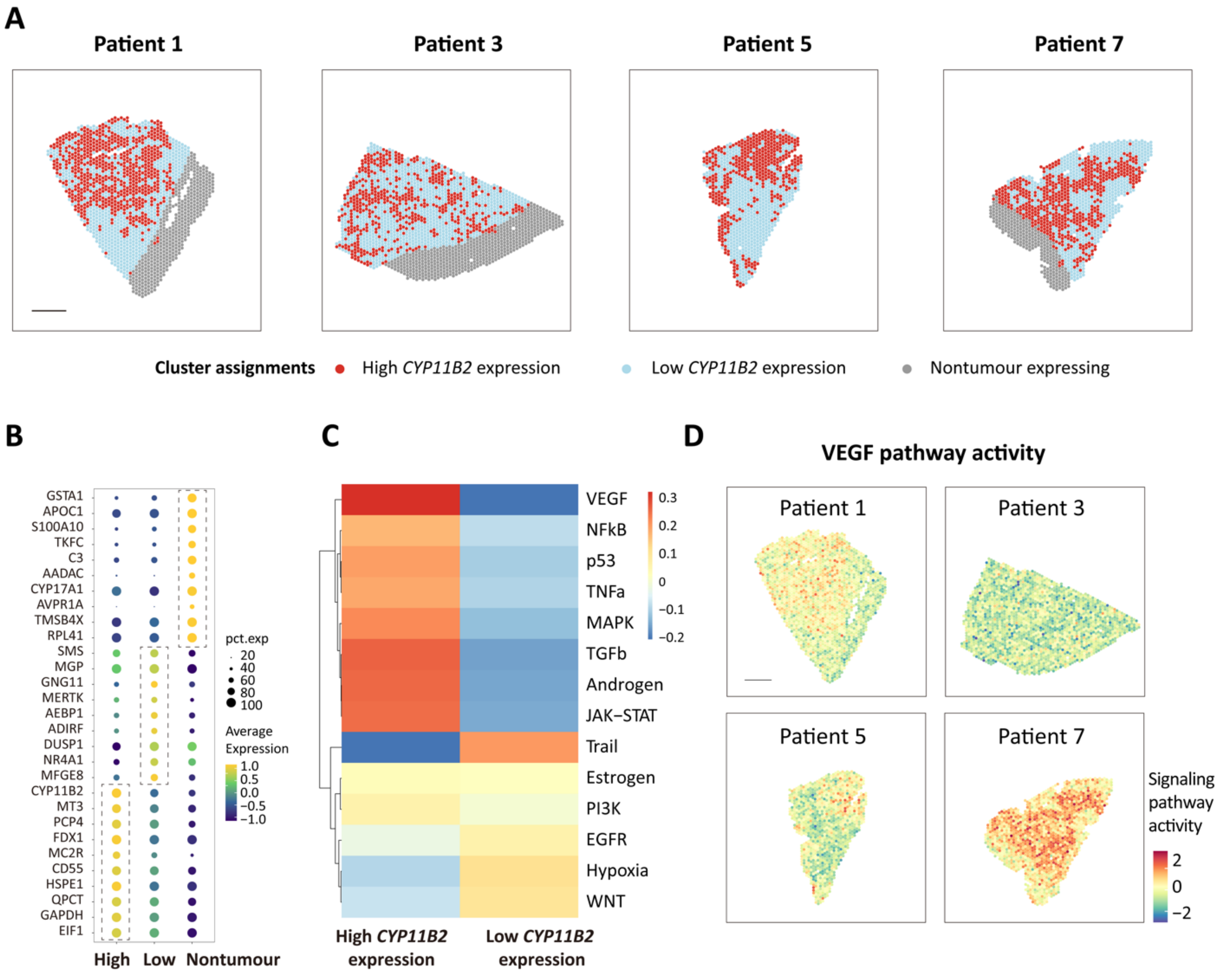

Figure S3 Heterogeneity of *CYP11B2* gene expression in *KCNJ5* mutated APAs.

A, *CYP11B2* expression levels in spatial transcriptomic spots of *KCNJ5* mutated APA. Spatial spots with high or low *CYP11B2* expression within the tumor area are indicated in red or blue, respectively, and spots from non-tumor regions are shown in grey. Scale bar, 1mm. **B**, bubble mapping of significantly differentially expressed genes associated with each of the 3 clusters of high or low *CYP11B2* expression or non-tumor area. Bubble size indicates the percentage of cluster spots expressing the corresponding gene and the color code indicates the average gene expression. **C**, heatmap showing the correlation *CYP11B2* expression levels and PROGENy pathway activity scores. Colour code indicates the corresponding signaling pathway activity. D, an example of the spatial distribution of the VEGF pathway in adrenal tissues that shows relative VEGF pathway activation in spatial spots with high *CYP11B2* expression.

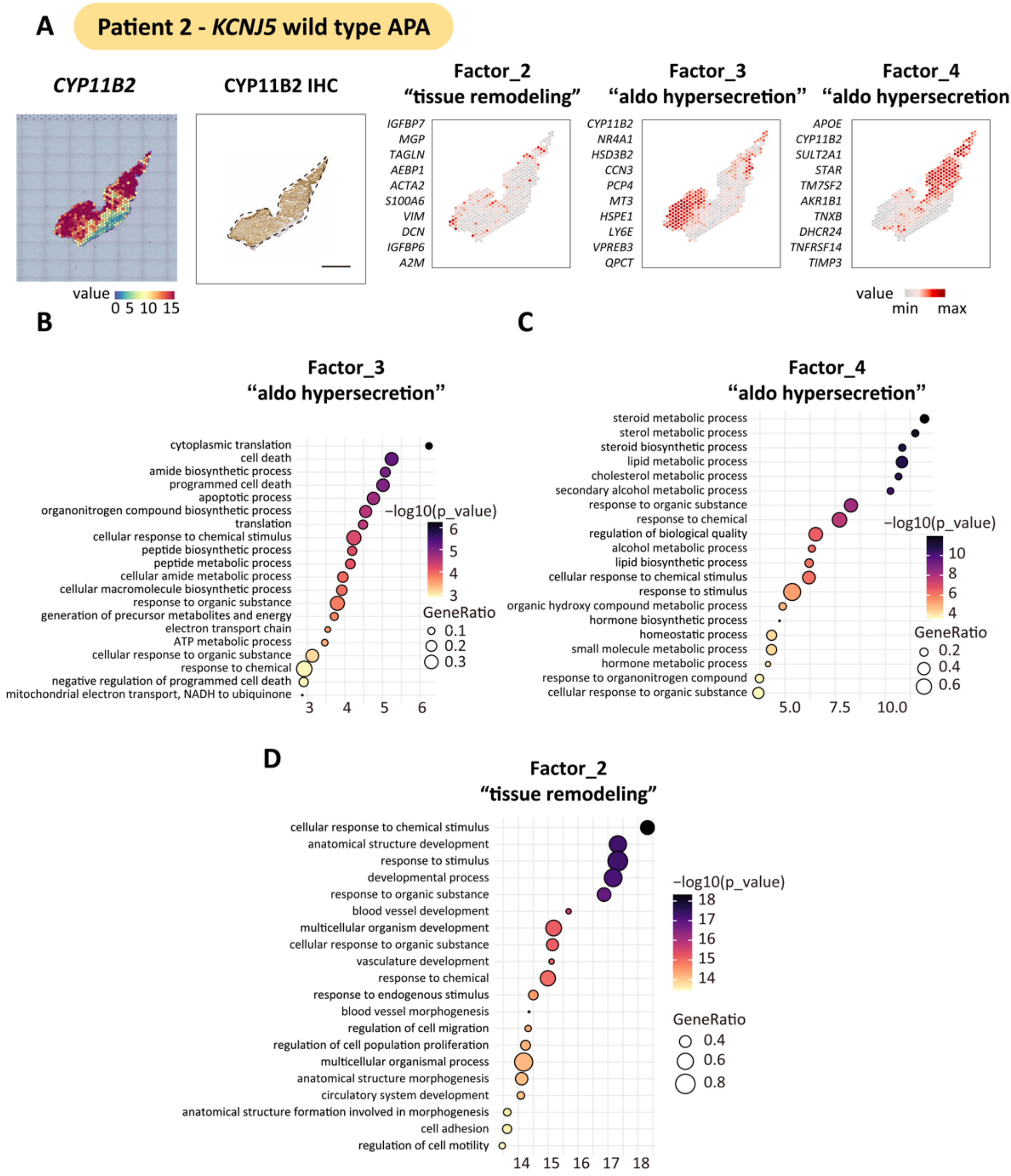

Figure S4 Intra-tumoral transcriptional heterogeneity of APAs without a *KCNJ5* mutation. NNMF expression-based analysis identified the top genes which define factors (transcriptionally distinct regions) in adrenal sections with an APA. The figure shows the analysis of patient 2 without a *KCNJ5* mutation. **A**, Spatial CYP11B2 and spatial distribution of the tumor-related factors, color-codes indicate gene expression levels. **Factors 2, 3 and 4,** are tumor-related factors: factor 3 and factor 4 comprise gene sets preferentially co-expressed in subsets of *CYP11B2* expressing tumor regions. *CYP11B2*, *NR4A1*, *HSD3B2*, *CCN3*, and *PCP4* were the top genes defining factor 3; *APOE*, *CYP11B2*, *SULT2A1*, *STAR*, and *TM7SF2* defined factor 4; conversely factor 2 defined tumor regions without CYP11B2 expression and was associated with tissue remodeling. Scale bar, 1 mm. **B-D**, Geno Ontology analysis showing enriched biological processes associated with factors related to “aldosterone hypersecretion” (factor 3 and factor 4) and “tissue remodeling” (factor 2).

Patient 2 - *KCNJ5* wild type APA

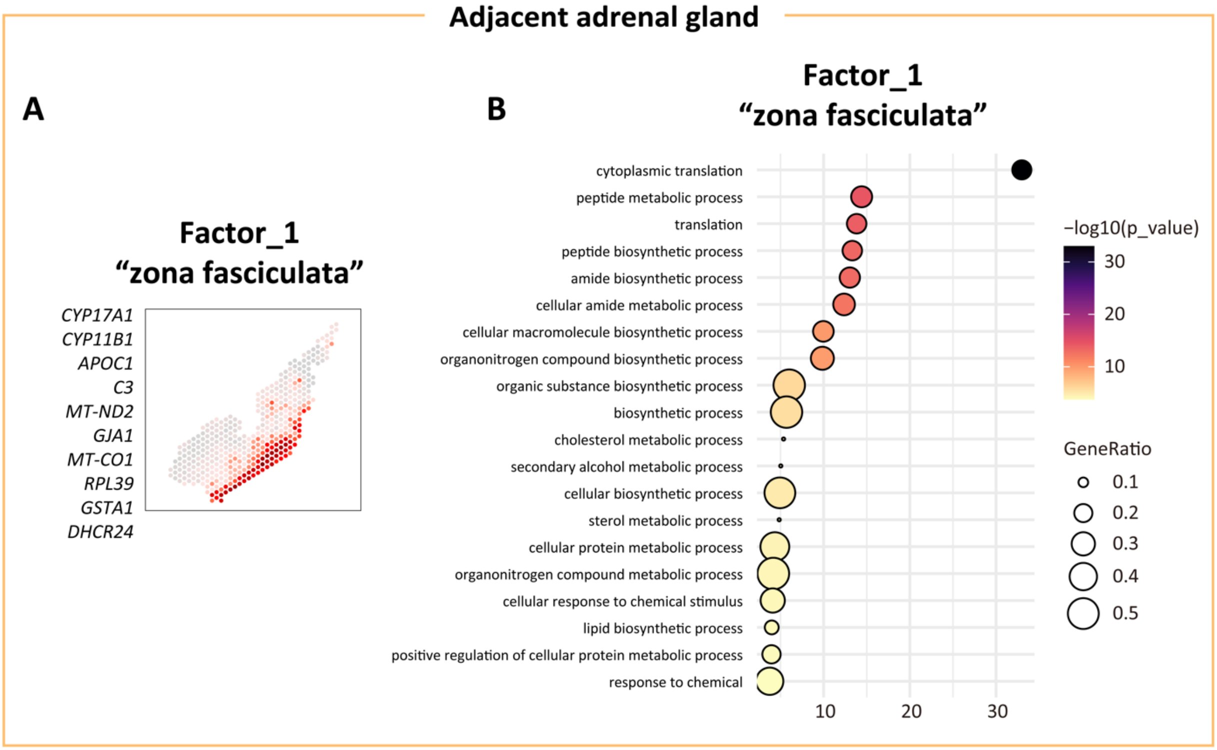

Figure S5. Non-negative matrix factorization reveals distinct molecular patterns in the adjacent adrenal gland of APAs without a *KCNJ5* mutation

A, Spatial distribution of the nontumor-related factor 1 and the associated top 10 annotated genes. Color-codes indicate gene expression levels. Factor 1 was characterized by zonation markers of the zona fasciculata (e.g., *CYP17A1* and *CYP11B1*). **B**, Geno Ontology analysis showing enriched biological processes associated with factor 1 related to "zona fasciculata" (factor 1, **Panel A**).

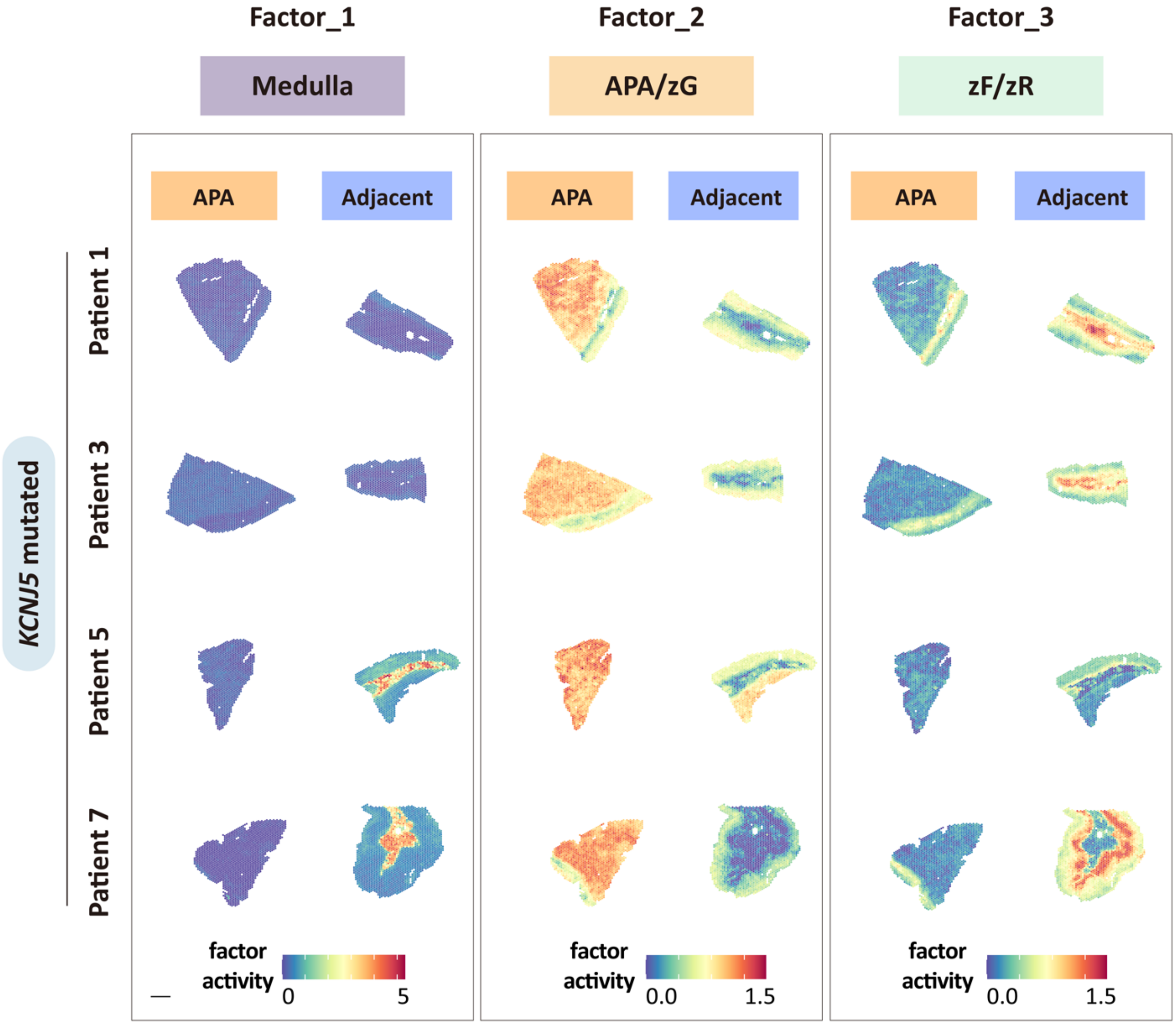

Figure S6. Non-negative matrix factorization to identify the spatial distribution of transcriptionally distinct regions in APAs with *KCNJ5* mutation and their adjacent cortex.
Spatial distribution of the 3 factors (transcriptionally distinct regions, factors 1-3) which distinguish zona fasciculata and zona reticularis, medulla, and a mixture of APA and zona glomerulosa in APA with a *KCNJ5* mutation. The color score assigned to spatial transcriptomics spots is based on the expression level of the genes which define each factor. Scale bar, 1mm.

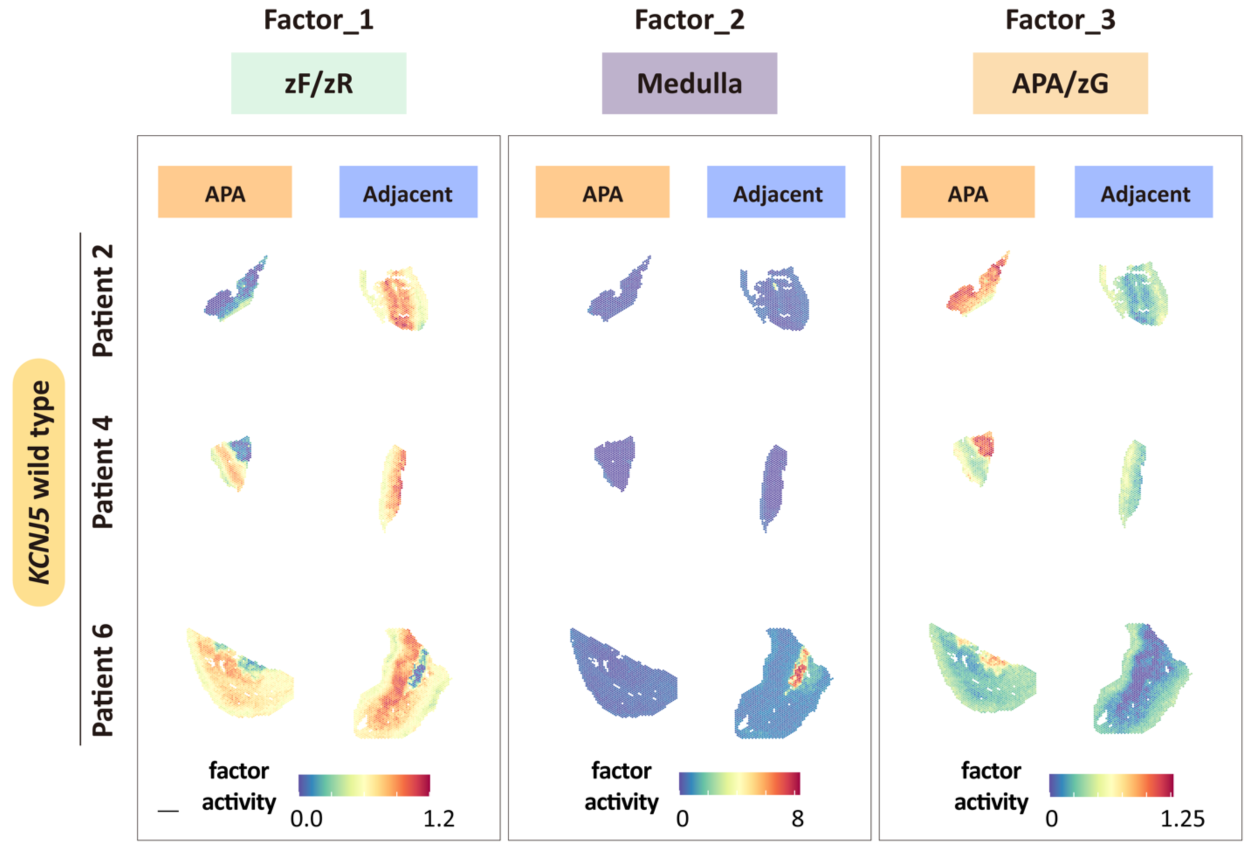

Figure S7. Non-negative matrix factorization to identify the spatial distribution of transcriptionally distinct regions in APAs without *KCNJ5* mutation and their adjacent cortex.
Spatial distribution of the 3 factors (transcriptionally distinct regions, factors 1-3) which distinguish zona fasciculata and zona reticularis, medulla, and a mixture of APA and zona glomerulosa in APA without a *KCNJ5* mutation. The color score assigned to spatial transcriptomics spots is based on the expression level of the genes which define each factor. Scale bar, 1mm.

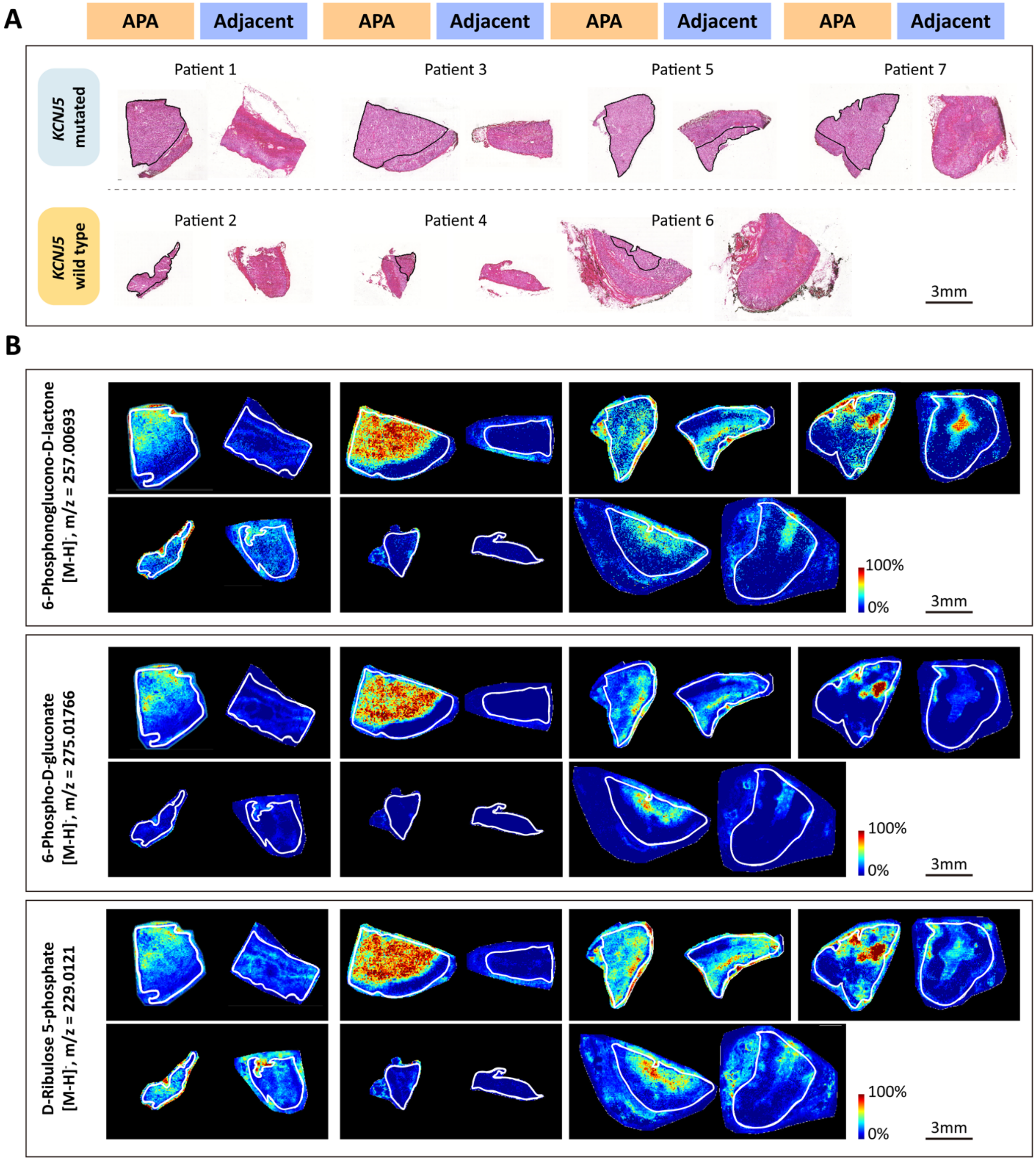

Figure S8. MALDI-MSI identification of upregulated oxidative pentose phosphate pathway metabolites in *KCNJ5* mutated APA compared with adjacent adrenal cortex.

A, Corresponding H&E-stained tissues of *KCNJ5* mutated (Upper) or *KCNJ5* wild type APA (Lower) and paired adjacent cortex for MALDI imaging. Outlined regions in black indicate APA tumor areas with positive CYP11B2 immunostaining. **B**, representative images of the spatial distribution of oxidative pentose phosphate pathway metabolites. Outlined regions in white indicate the borders of the tissue section.

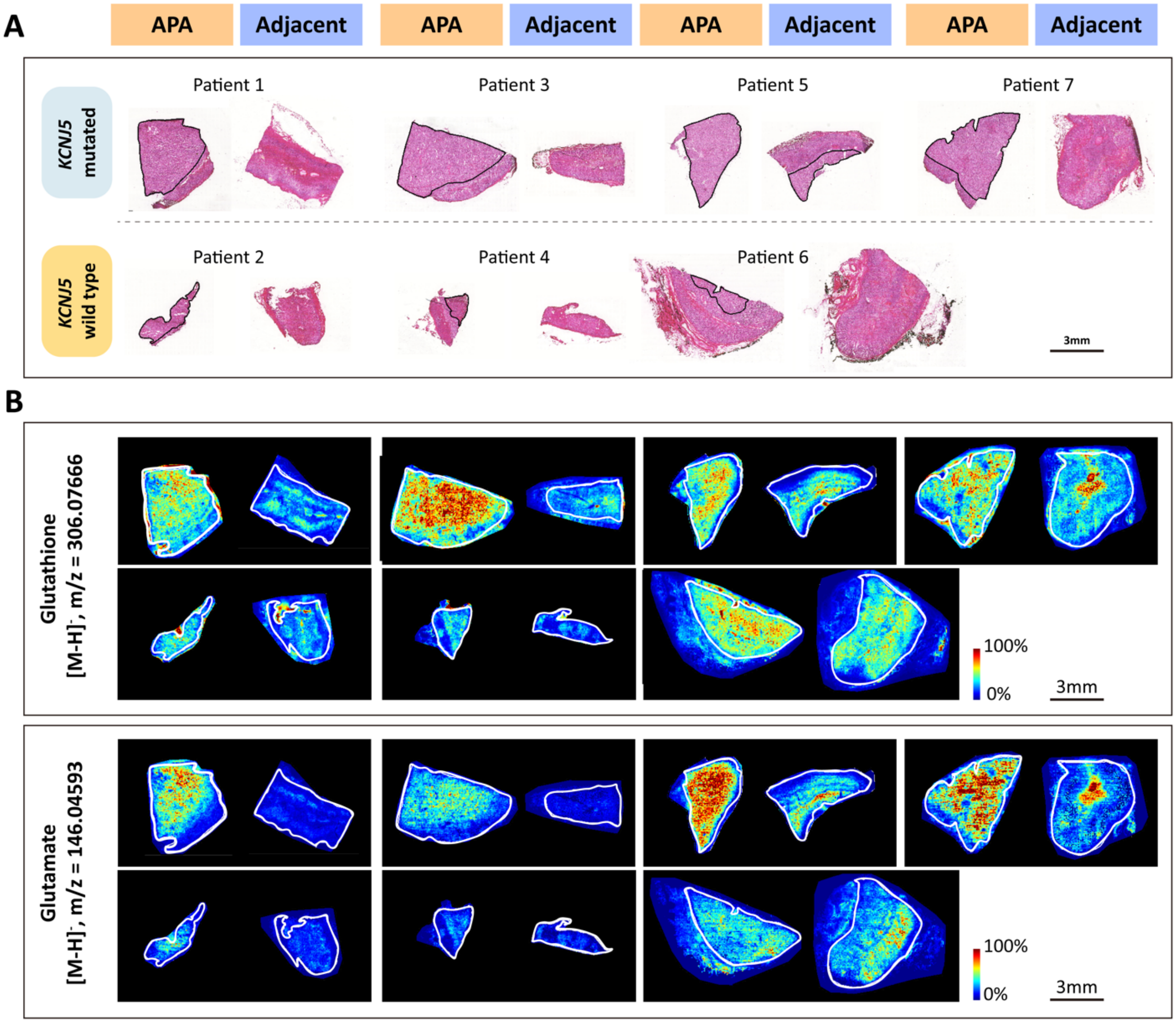

Figure S9. MALDI-MSI identification of upregulated glutathione metabolism metabolites in *KCNJ5* mutated APA compared with adjacent adrenal cortex.

A, corresponding H&E-stained tissues of *KCNJ5* mutated APA (Upper) or *KCNJ5* wild type APA (Lower) and adjacent adrenal gland for MALDI MSI. Outlined regions in black indicate APA tumor areas with positive CYP11B2 immunostaining. **B**, representative images showing spatial distribution of glutathione metabolism metabolites (glutathione and glutamate). Outlined regions in white indicate the borders of the tissue section.

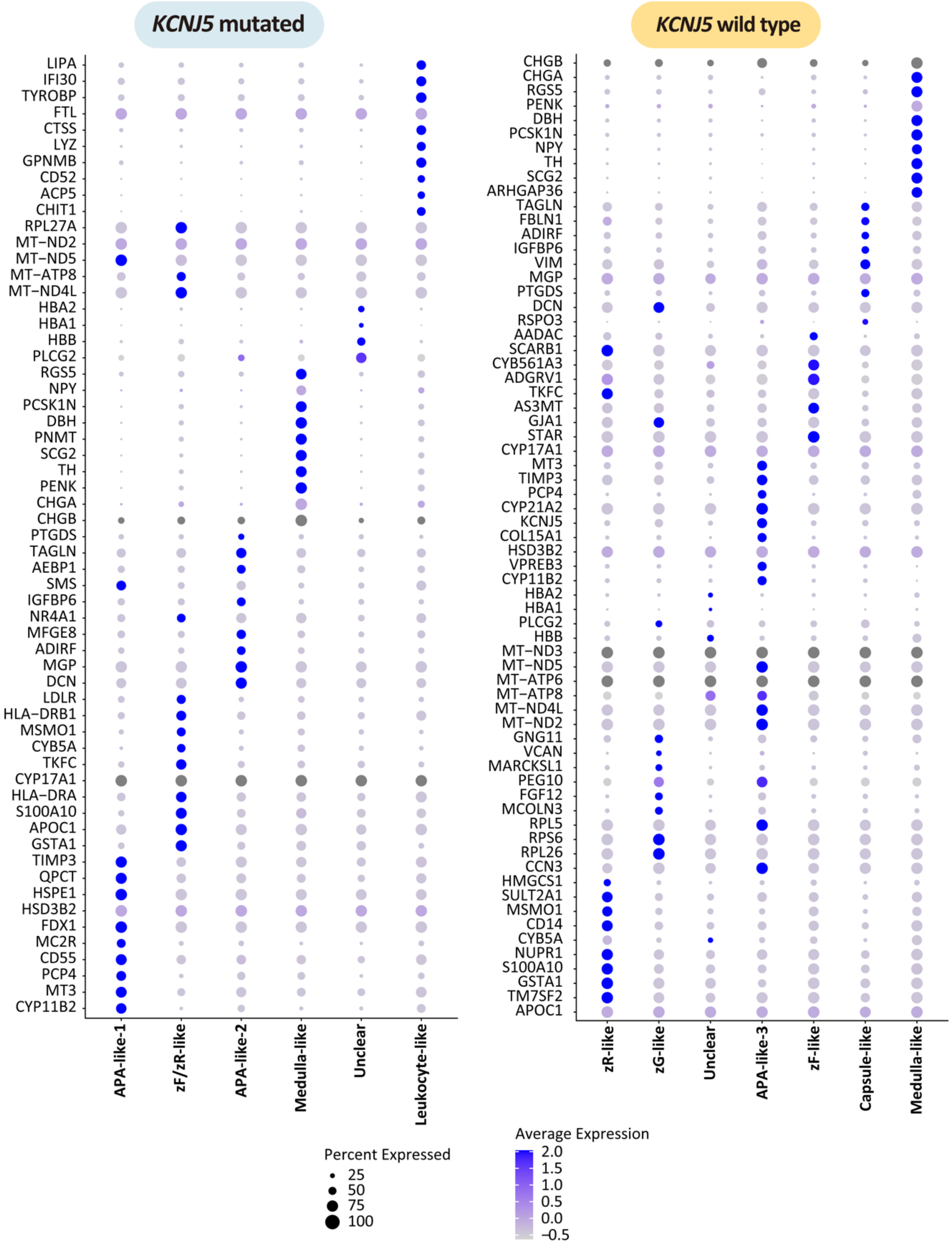

Figure S10. Identification of transcriptomic subpopulations
Bubble plot showing the top 10 differentially expressed genes within each transcriptomic cluster shown in Figure 6 (main manuscript) stratified by APA genotype.

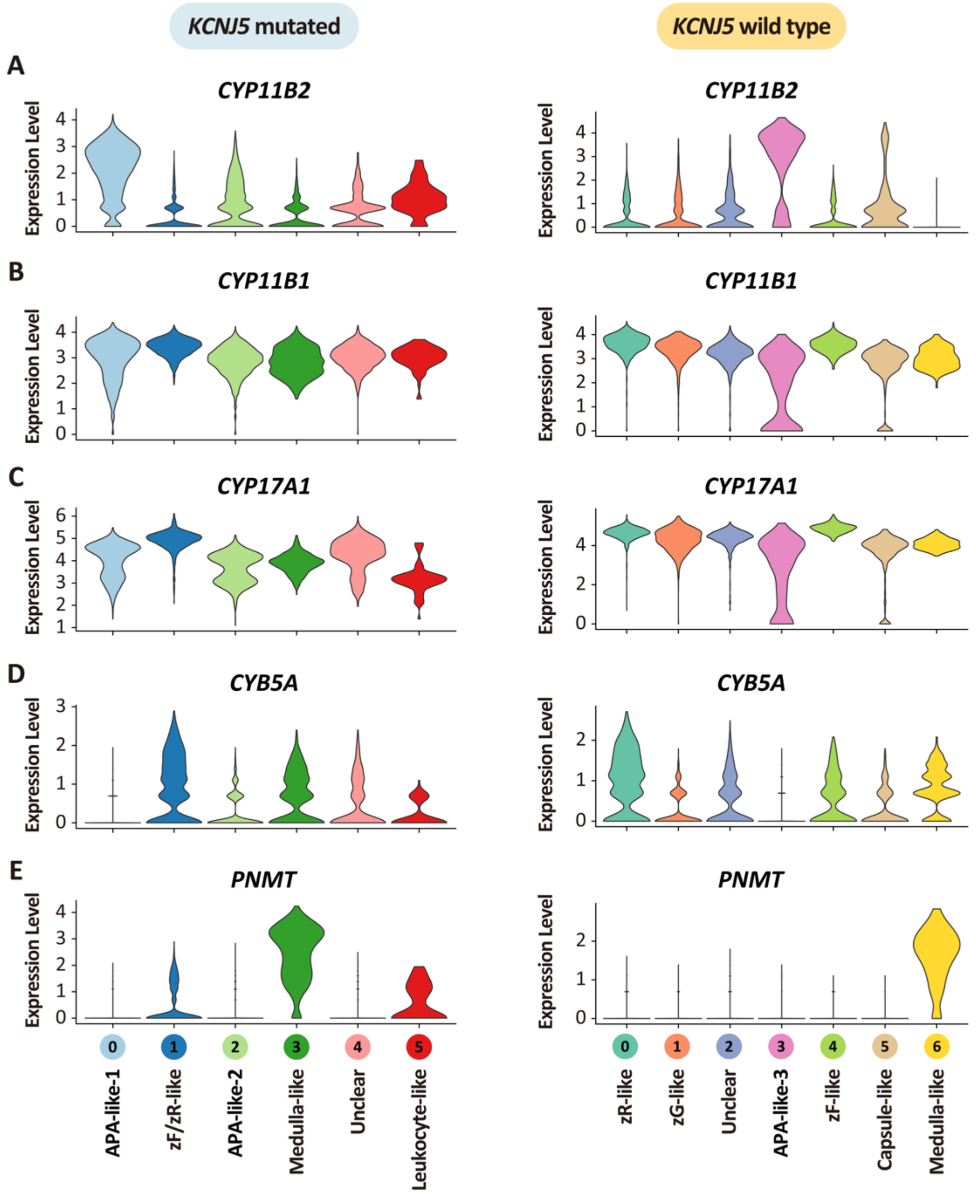

Figure S11. **Expression of steroidogenic enzyme genes in adrenal cell types.**
Violin plots showing the expression of genes encoding steroidogenic enzyme known to be expressed in a cell-type specific manner. **A**, *CYP11B2* gene was selectively enriched in APA-like clusters (APA-like-1 in patients with APA-*KCNJ5*^{MUT} (Left); APA-like-3 in patients with APA-*KCNJ5*^{WT} (Right)). **B-D**, *CYP11B1*, *CYP17A1*, and *CYB5A* genes were enriched in regions with a high abundance of zona fasciculata and zona reticularis cells (zF/zR-like cluster in patients with APA-*KCNJ5*^{MUT} (Left); zR-like and zF-like clusters in patients with APA-*KCNJ5*^{WT} (Right)). **E**, PNMT gene was enriched in medulla-like clusters in patients with APA-*KCNJ5*^{MUT} and patients with APA-*KCNJ5*^{WT}, respectively. Left and right panels indicate adrenal tissues from patients with a *KCNJ5* mutation (Left) or without a *KCNJ5* mutation (Right)). The fill color of the violin plots indicates the subpopulations identified in Figure 6 (main text). APA, aldosterone-producing adenoma; zG, zona glomerulosa; zF, zona fasciculata; zR, zona reticularis.

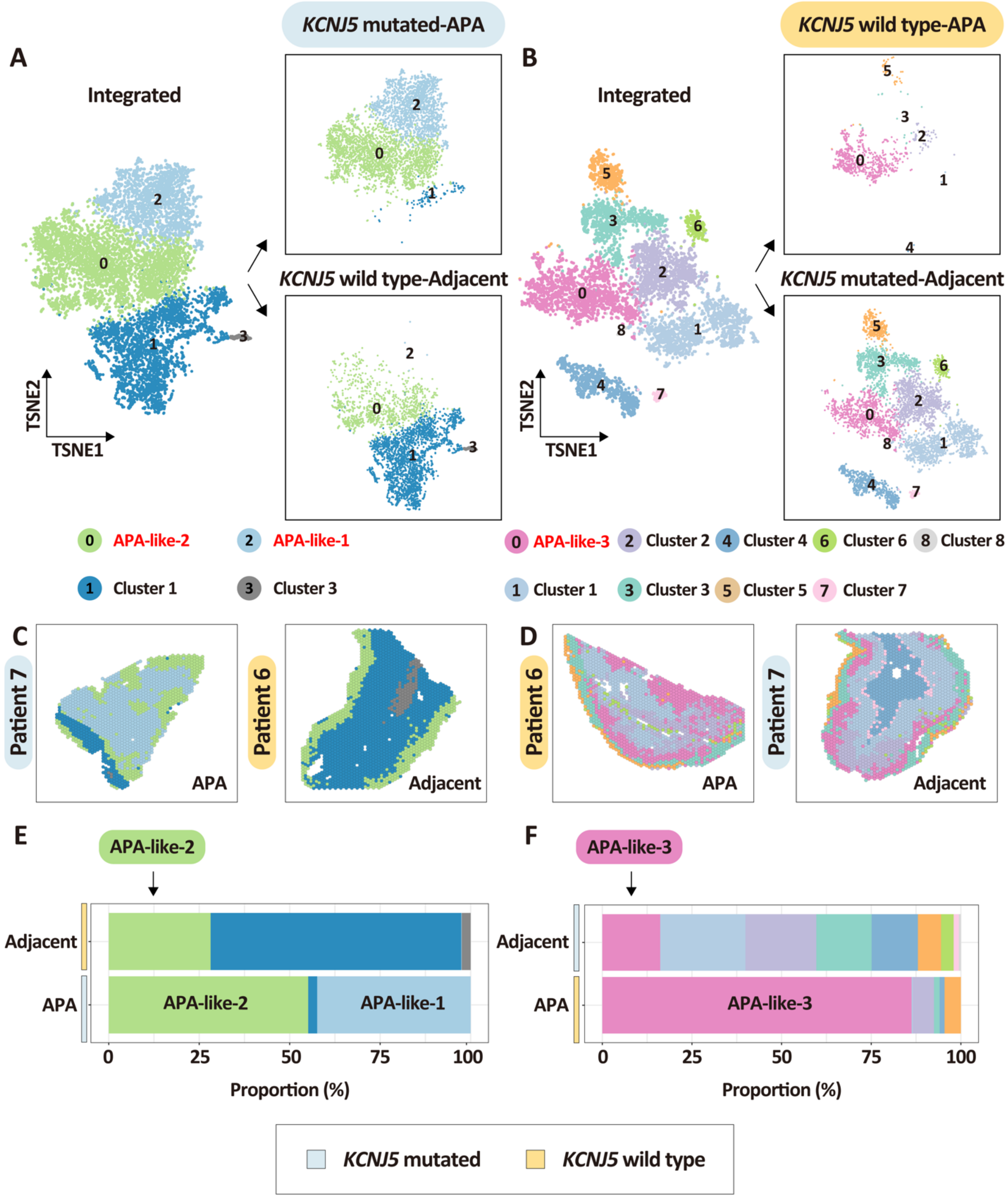

Figure S12. The validation of APA-like subpopulations through comparisons of non-matching tumor-adjacent cortex pairs.

We excluded potential excessive interpretation of the algorithm used by integrative analysis of *KCNJ5*-mutated APAs compared with the adjacent adrenal cortex of APAs without a *KCNJ5* mutation (**A**, **C**, and **E**) and of APAs without a *KCNJ5* mutation compared with the adjacent adrenal cortex of APAs with a *KCNJ5* mutation (**B**, **D**, and **F**). **A-B**, t-distributed stochastic neighbor embedding representations of the integrated spatial transcriptomes of APAs and adjacent adrenal tissues stratified by APA-*KCNJ5* mutation status and tissue type. **A** and **B** show integrated spatial transcriptomic spots from APAs and adjacent adrenal tissues (left image of **A** and **B**) as well as separated into APAs (boxed image, top right of **A** and **B**) and adjacent tissues (boxed image, bottom right of **A** and **B**). Colors represent transcriptome subpopulations as indicated. APA-like clusters are marked in red writing. **A**, APA-*KCNJ5*^{MUT} (*n*= 4) and adjacent adrenal cortex of APA-*KCNJ5*^{WT} (*n* = 3). **B**, APA-*KCNJ5*^{WT} (*n* = 3) and adjacent adrenals of APA-*KCNJ5*^{MUT} (*n* = 4). **C-D**, Representative spatial transcriptomics sections showing the distribution of spots in APAs and adjacent adrenals from patient 7 with a *KCNJ5* mutation (male) and patient 6 without a *KCNJ5* mutation (female). **E-F**, stacked plots showing the proportion of each transcriptome cluster in APAs and non-matching adjacent adrenals. **E**, APAs-*KCNJ5*^{MUT} and adjacent adrenals of APAs-*KCNJ5*^{WT}. **F**, APAs-*KCNJ5*^{WT} and adjacent adrenals of APAs-*KCNJ5*^{MUT}.

Note that in panel **C**, the APA-like-1 and APA-like-2 subpopulations in APA-*KCNJ5*^{MUT} of patient 7 (cluster 2 and cluster 0) *versus* the adjacent cortex to the APA-*KCNJ5*^{WT} of patient 6 displayed a similar spatial distribution as compared to its own corresponding paired adjacent cortex shown in **Figure 6C** (main manuscript). Likewise, in panel **D**, the APA-like 3 subpopulation in APA-*KCNJ5*^{WT} of patient 6 (cluster 0) *versus* the adjacent cortex to the APA-*KCNJ5*^{MUT}of patient 7 displayed a similar spatial distribution as compared to its own corresponding paired adjacent cortex shown in **Figure 6D** (main manuscript). Also note that subpopulations APA-like 2 and APA-like 3 are common to tumor areas and the adjacent tissue in this analysis of non-matched APAs and adjacent cortex to an APA of different genotype and in the analysis of APA and paired adjacent cortex from the same patient in **Figure 6E and F** (main manuscript). In contrast, APA-like 1 is present only in the tumor tissue of APA-*KCNJ5*^{MUT} but is undetectable in the adjacent adrenal cortex to APA-*KCNJ5*^{WT} (**E**) but present in its paired adjacent cortex **Figure 6E** (main manuscript).